Heat transport in liquid water from first-principles and deep neural network simulations

Davide Tisi, Linfeng Zhang, Riccardo Bertossa, Han Wang, Roberto Car, and Stefano Baroni

Heat transport in liquid water from first-principles and deep-neural-network simulations

Davide Tisi,[1] Linfeng Zhang,[2] Riccardo Bertossa,[1] Han Wang,[3] Roberto Car,[2, 4] and Stefano Baroni[1, 5]

[1] *SISSA – Scuola Internazionale Superiore di Studi Avanzati, 34136 Trieste, Italy*
[2] *Program in Applied and Computational Mathematics,*
Princeton University, Princeton, NJ 08544, USA
[3] *Laboratory of Computational Physics, Institute of Applied Physics and Computational Mathematics,*
Huayuan Road 6, Beijing 100088, People's Republic of China
[4] *Department of Chemistry, Department of Physics,*
and Princeton Institute for the Science and Technology of Materials,
Princeton University, Princeton, NJ 08544, USA
[5] *CNR Istituto Officina dei Materiali, SISSA unit, 34136 Trieste, Italy*
(Dated: November 28, 2021)

We compute the thermal conductivity of water within linear response theory from equilibrium molecular dynamics simulations, by adopting two different approaches. In one, the potential energy surface (PES) is derived on the fly from the electronic ground state of density functional theory (DFT) and the corresponding analytical expression is used for the energy flux. In the other, the PES is represented by a deep neural network (DNN) trained on DFT data, whereby the PES has an explicit local decomposition and the energy flux takes a particularly simple expression. By virtue of a gauge invariance principle, established by Marcolongo, Umari, and Baroni, the two approaches should be equivalent if the PES were reproduced accurately by the DNN model. We test this hypothesis by calculating the thermal conductivity, at the GGA (PBE) level of theory, using the direct formulation and its DNN proxy, finding that both approaches yield the same conductivity, in excess of the experimental value by approximately 60%. Besides being numerically much more efficient than its direct DFT counterpart, the DNN scheme has the advantage of being easily applicable to more sophisticated DFT approximations, such as meta-GGA and hybrid functionals, for which it would be hard to derive analytically the expression of the energy flux. We find in this way, that a DNN model, trained on meta-GGA (SCAN) data, reduce the deviation from experiment of the predicted thermal conductivity by about 50%, leaving the question open as to whether the residual error is due to deficiencies of the functional, to a neglect of nuclear quantum effects in the atomic dynamics, or, likely, to a combination of the two.

I. INTRODUCTION

Heat transport plays an important role in many areas of science, such as, e.g., materials and planetary sciences, with major impact on technological issues, such as energy saving and conversion, heat dissipation and shielding, etc. Numerical studies of heat transport at the molecular scale often rely on Boltzmann's kinetic approach [1–4]. This is adequate when the relaxation processes are dominated by binary collisions, as in the case of dilute gases of particles, such as atoms or molecules, or of quasi-particles, such as phonons in crystalline solids. A more general approach to calculate the transport coefficients is provided by simulations of the molecular dynamics (MD), either directly via non-equilibrium MD [5–8], or in combination with Green-Kubo (GK) theory of linear response [5, 6, 9, 10] via equilibrium MD.

Much progress has been made in recent years to develop *ab initio* approaches to heat transport based on electronic density functional theory (DFT). Some schemes used *ad hoc* ingredients, such as a (rather arbitrary) quantum-mechanical definition of the atomic energies [11]. Other schemes used a definition of the energy flux based on the normal-mode decomposition of the atomic coordinates and forces, which is only possible in crystalline solids [12]. In this work we follow the for-mulation of Marcolongo, Umari, and Baroni (MUB) [13], who derived a general DFT expression for the adiabatic energy flux, based on a *gauge invariance* principle for the transport coefficients [13, 14]. The MUB approach made *ab initio* simulations of heat transport possible, not only for crystalline materials, but also for disordered systems, like liquids and glasses, albeit at the price of lengthy and costly simulations. Progress in statistical techniques for the analysis of the flux time series [15, 16] made possible to achieve 10% accuracy in the calculated thermal conductivity with simulations of a few dozen to a few hundred picoseconds. Still the computational burden of *ab initio* MD, where the potential energy surface (PES) is generated on the fly from DFT, is heavy and requires access to high performance computer platforms for substantial wall-clock times (see, e.g., Appendix F of Ref. [17] for details on the computational cost of a MUB calculation).

In the last decade, a combination of standard electronic-structure methods, based on DFT, and new machine-learning techniques have allowed the construction of inter-atomic potentials possessing quantum mechanical accuracy at a cost that is only marginally higher than that of classical force fields. All the machine learned potentials, which are represented either by a deep-neural network (DNN) [18–21] or by a Gaussian-process [22],

use a local decomposition of the total potential energy of the system in terms of atomic contributions, which makes straightforward to define the energy flux, or current, from which to compute the heat conductivity via GK theory.

Here we adopt the recently developed deep potential (DP) framework [21, 23]. DP molecular dynamics (DPMD) simulations have been used successfully to study bulk thermodynamic properties beyond the reach of direct DFT calculations [24–30], as well as dynamic properties like mass diffusion in solid state electrolytes [31, 32], thermal transport properties in silicon [33], infrared spectra of water and ice [34] and Raman spectra of water [35]. In the present work, we report calculations of the thermal conductivity (κ) of water, a molecular liquid, from both direct DFT and DPMD simulations. The close correspondence of the conductivities predicted with the two approaches validates DPMD against the results obtained from the MUB current. We adopt two popular DFT approximations: the PBE generalized gradient approximation (GGA) [36] and the strongly constrained and appropriately normed (SCAN) meta-GGA [37]. The SCAN functional describes water more accurately than PBE, relative to which it reduces the covalent character of the hydrogen bond and correctly predicts that the liquid is denser than the solid [38]. However, expressions for the energy density and fluxes are not currently available for the SCAN functional, and its inherent complexity makes hard to derive usable analytical expressions for these quantities. Because of that, we used PBE to validate our methodology. Our results show that direct DFT simulations based on the PBE functional, and simulations based on the corresponding DP model are in good agreement with each other, but distinctly overestimate the thermal conductivity relative to experiment. This outcome likely reflects the well known tendency of PBE to overestimate the strength of the hydrogen bonds, enhancing short-range order and making liquid water more "solid-like" and prone to freezing [39]. DPMD simulations trained on SCAN-DFT reduce substantially the error of the heat conductivity predicted by PBE, but do not eliminate it, thus leaving open the question as to its origin, which is possibly due to residual deficiencies of the functional, to nuclear quantum effects ignored in the MD equations of motion, or, likely, to a combination of the two.

The paper is organized as follows. In Section II, we recall the main aspects of the GK theory, along with two basic invariance principles of thermal transport that allow us, among other things, to define the MUB-DFT energy flux. In Section III, we describe the DP model, derive the corresponding expression for the energy flux, and discuss the impact of the invariance principles within a DNN simulation framework. In Section IV, we benchmark our DNN methodology against *ab initio* MD simulations of liquid water at the PBE level of theory [36]. Having proved that DPMD trustfully reproduces *ab initio* results, in Section V, we take advantage of the simple DNN expression for the heat current to compute the thermal transport coefficients of liquid water at the SCAN meta-GGA level of theory. Section VI contains our conclusions.

II. THEORY

GK theory of linear response [9, 10] provides a rigorous and elegant framework to compute the atomic contribution to the thermal conductivity, κ, of extended systems, in terms of the stationary time series of the energy flux [40], $\boldsymbol{J}^e$, evaluated at thermal equilibrium with MD. For an isotropic system of N interacting particles, the GK expression for the heat conductivity reads:

$$\kappa = \frac{V}{3k_B T^2} \int_0^\infty \langle \boldsymbol{J}^e(\Gamma_t) \cdot \boldsymbol{J}^e(\Gamma_0) \rangle dt, \qquad (1)$$

where Γ_t indicates the time evolution of a point in phase space from the initial condition Γ_0. The definition of the energy current in Eq. (1) is the key ingredient for the computation of κ. This definition relies in general on extensivity, which allows the total, conserved, energy of an isolated system to be broken up into local contributions. In a classical setting, this is conveniently achieved by expressing the total energy as a sum of atomic energies, $\epsilon_n = \frac{1}{2} M_n \boldsymbol{v}_n^2 + w_n$, where M_n and $\boldsymbol{v}_n$ are atomic masses and velocities, and w_n are suitably defined atomic potential energies, *vide infra*. When this is done, the energy flux can be written as

$$\boldsymbol{J}^e(t) = \frac{1}{V} \sum_n \left[\boldsymbol{v}_n \epsilon_n - \sum_m (\boldsymbol{r}_n - \boldsymbol{r}_m) \frac{\partial w_m}{\partial \boldsymbol{r}_n} \cdot \boldsymbol{v}_n \right], \quad (2)$$

where $\boldsymbol{r}_n$ are atomic positions and n and m run over all the atoms in the system [14, 41, 42]. In the case of pairwise interactions, for instance, it can be assumed that $w_n = \frac{1}{2} \sum_{m \neq n} w(|\boldsymbol{r}_m - \boldsymbol{r}_n|)$. For a general many-body interaction, a similar partition of the total energy into local contributions is also possible. In a quantum-mechanical setting, it is not possible to uniquely define the atomic energies appearing in Eq. (2), and the total energy of a system can at most be expressed in terms of an energy *density*, which is also ill-defined. For instance, the electrostatic energy of a continuous charge-density distribution can be expressed as either one half the integral of the density times the potential, or of $\frac{1}{8\pi}$ the squared modulus of the field; by the same token, the kinetic energy of a quantum particle can be expressed as the integral of the squared modulus of the gradient of its wave-function, or of the negative of the product of the wave-function and its Laplacian. For this reason, it has long been feared that no quantum-mechanical expressions for the heat conductivity could be obtained from first principles [43]. Actually, although not generally fully appreciated, this same problem arises with classical force fields as well, because classical atomic energies themselves are ill-defined. In the example of pair-wise interactions any different partition

of the interaction energy of the nm pair into individual atomic contributions would be equally acceptable and, yet, would lead to a different expression for the energy flux [14].

This long-standing problem was solved for good only recently with the introduction of a *gauge invariance* principle for the transport coefficients [13, 14, 44], as explained in the following subsections.

A. Gauge invariance

In order to introduce, and understand, the recently discovered *gauge* and *convective* invariance principles for the transport coefficients, it is useful to define the concept of *diffusive* flux. A flux is said to be diffusive if its GK integral, as defined in Eq. (1), is different from zero; the flux is said to be non-diffusive otherwise. Gauge invariance states that the addition of any linear combination of *non-diffusive* fluxes to a *diffusive* one does not affect the value of the conductivity calculated with the GK formula, Eq. (1). This principle got this name because it results from a kind of gauge invariance of conserved densities, according to which any such density is only defined up to the divergence of a bounded vector field. This is so because the volume integral of such a divergence is irrelevant in the thermodynamic limit, and, thus, does not contribute to the value of the conserved quantity. This divergence would, in turn, result in the addition of a non-diffusive term to the flux of the conserved quantity, thus not affecting the value of the transport coefficient.

B. Convective invariance

In general, a system made of M atomic species (an M-*component system*) has $M + 4$ conserved quantities (the number of atoms of each species, the energy, and the three components of the momentum). The energy and atomic-number currents are vector quantities, whereas the momentum currents are 3×3 (stress) tensors, which do not couple with the former in a rotationally invariant system. The total momentum is not only a conserved quantity by itself, but is also a linear combination of the volume integral of the atomic-number currents (*atomic-number fluxes*). This reduces the number of independent mass fluxes from M to $M - 1$. We conclude that, when dealing with an M-component system, the conserved quantities relevant to heat transport are the total energy and the total numbers (or masses) of each one of the $M - 1$ independent atomic components, which, in the linear regime, are related to each other by Onsager's phenomenological relations:

$$\boldsymbol{J}^i = \sum_{j=0}^{M-1} \Lambda^{ij} \boldsymbol{F}^j, \qquad (3)$$

where $\boldsymbol{F}^j$ is the thermodynamic force associated to the $j - th$ conserved quantity being transported. In Eq. (3) the energy flux is identified as the zero-th term, the remaining $M-1$ fluxes being any linearly independent combinations of the mass fluxes, and the Λ coefficients are expressed by the GK integrals:

$$\Lambda^{ij} = \frac{V}{k_B} \int_0^\infty \langle \boldsymbol{J}^i(\Gamma_t) \boldsymbol{J}^j(\Gamma_0) \rangle dt. \qquad (4)$$

In the multi-component case, the heat conductivity is defined as the ratio between the energy current and the negative of the temperature gradient, *when all the mass currents vanish*. With some simple algebra, we arrive at the expression [16]:

$$\kappa = \frac{1}{T^2} \left[\Lambda^{00} - \sum_{i,j=1}^{M-1} \Lambda^{0i} (\Lambda_{M-1}^{-1})^{ij} \Lambda^{j0} \right], \qquad (5)$$

where Λ_{M-1}^{-1} is the inverse of the $(M-1) \times (M-1)$ mass block of the Onsager matrix. The expression in square brackets in Eq. (5) is called the *Schur complement* of the mass block in the Onsager matrix, and is nothing but the inverse of the 00 element of the inverse Onsager matrix.

By combining the definition of Λ with Eq. (5), one can demonstrate by a straightforward substitution that the heat conductivity is invariant with respect to the addition of any linear combination of mass fluxes to the energy flux: $\boldsymbol{J}^0 \to \boldsymbol{J}^0 + \sum_{i=1}^{M-1} c^i \boldsymbol{J}^i$. This is the transformation the energy flux undergoes when the energies of all the atoms of the same chemical species are shifted by the same amount, such as it occurs, *e.g.*, when passing from an all-electron to a pseudo-potential representation of the electronic structure, or when changing pseudo-potentials. This property has been called *convective invariance* [16]

Molecular fluids, such as undissociated water, deserve a special comment. In this case, one demonstrates that, as the atoms in each molecule do not diffuse relative to the center of mass of the molecule, all the independent atomic mass/number fluxes are non-diffusive. Therefore, energy can be assumed to be the only conserved flux relevant to heat transport, as it is the case for strictly one-component fluids [13].

Notwithstanding gauge and convective invariance, the statistical noise affecting the estimate of the heat conductivity does depend on the energy flux of the non-diffusing components that are added to the diffusive energy flux. Gauge invariance can then be leveraged to tune the optimal linear combination of non-diffusive fluxes to minimize the statistical error on the heat conductivity. In order to achieve this goal, it is expedient to consider the transport coefficient as the zero-frequency value of $S(\omega)$, the flux power spectrum, which is given, in the multi-component case, by:

$$S(\omega) = \frac{V}{2k_B T^2} \frac{1}{[\bar{S}^{-1}(\omega)]^{00}}, \qquad (6)$$

where $[\bar{S}^{-1}(\omega)]^{00}$ is the 00 element of the inverse of the matrix defined by:

$$\bar{S}^{ij}(\omega) = \int_{-\infty}^{\infty} \langle \boldsymbol{J}^i(\Gamma_t)\boldsymbol{J}^j(\Gamma_0)\rangle e^{-i\omega t} dt. \qquad (7)$$

In molecular fluids, all mass fluxes are non diffusive [13] and energy is the only conserved quantity relevant to heat transport. Therefore, we actually have $S(0) = \frac{V}{2k_B T^2}\bar{S}^{00}(0)$ and, strictly speaking, no multi-component analysis would be needed. However, data analysis is greatly facilitated when the power spectrum is as smooth as possible (to be precise, when the number of inverse Fourier coefficients of the logarithm of the spectrum are as few as possible [15]). For this reason, it may be convenient to complement the diffusive energy flux with a number of non-diffusive ones, which, while not altering the value of the spectrum in Eq. (6) at $\omega = 0$, decrease the total power, thus easing data analysis [16, 42, 44, 45].

C. The MUB DFT adiabatic energy flux

Gauge invariance solves the problem of the alleged indeterminacy of the quantum-mechanical adiabatic energy flux, thus providing a rigorous derivation of its expression within DFT, without introducing any ad-hoc ingredients [13]. Within the local density (LDA) and generalized gradient (GGA) approximations of DFT, the MUB expression for the DFT energy flux [13, 17] is:

$$\boldsymbol{J}^{MUB} = \boldsymbol{J}^{KS} + \boldsymbol{J}^H + \boldsymbol{J}^0 + \boldsymbol{J}^n + \boldsymbol{J}^{XC}, \qquad (8)$$

where

$$\boldsymbol{J}^{KS} = \sum_v \left(\langle \varphi_v|\hat{\boldsymbol{r}}\hat{H}^{KS}|\dot{\varphi}_v\rangle + \varepsilon_v\langle\dot{\varphi}_v|\hat{\boldsymbol{r}}|\varphi_v\rangle \right),$$

$$\boldsymbol{J}^0 = \sum_{n\boldsymbol{L}}\sum_v \langle \varphi_v|(\hat{\boldsymbol{r}} - \boldsymbol{r}_n - \boldsymbol{L})(\boldsymbol{v}_n \cdot \nabla_{n\boldsymbol{L}}\hat{v}^0)|\varphi_v\rangle,$$

$$\boldsymbol{J}^n = \sum_n \left[\boldsymbol{v}_n e_n^0 - \sum_{\boldsymbol{L}\neq 0}\boldsymbol{L}(\boldsymbol{v}_n \cdot \nabla_{n\boldsymbol{L}}w_n^Z) \right. \qquad (9)$$

$$\left. + \sum_{m\neq n}\sum_{\boldsymbol{L}}(\boldsymbol{r}_n - \boldsymbol{r}_m - \boldsymbol{L})(\boldsymbol{v}_m \cdot \nabla_{m\boldsymbol{L}}w_n^Z) \right]$$

$$\boldsymbol{J}^H = \frac{1}{4\pi e^2}\int \dot{v}^H(\boldsymbol{r})\nabla v^H(\boldsymbol{r})d\boldsymbol{r},$$

$$\boldsymbol{J}^{XC} = \begin{cases} 0 & \text{(LDA)} \\ -\int n(\boldsymbol{r})\dot{n}(\boldsymbol{r})\partial\epsilon^{\text{GGA}}(\boldsymbol{r})d\boldsymbol{r} & \text{(GGA)}, \end{cases}$$

where $\boldsymbol{r}_n$, $\boldsymbol{v}_n$, and $w_n^Z = 1/2\sum'_{m\neq n}(Z_m Z_n/|\boldsymbol{r}_n - \boldsymbol{r}_m|)$ are ionic positions, velocities, and electrostatic energies, respectively, Z_n are ionic charges, and $\sum'$ includes all the atoms in the cell and their periodic images; $\hat{H}^{KS}$ is the instantaneous Kohn–Sham (KS) Hamiltonian, φ_ν and ε_ν are the occupied eigenfunctions and corresponding eigenvalues, and $\rho(\boldsymbol{r}) = \sum_\nu |\varphi_\nu(\boldsymbol{r})|^2$ is the ground-state electron-density distribution; v_H, v_{XC} are Hartree and exchange-correlation (XC) potentials; $\boldsymbol{L}$ is a lattice vector, $\nabla = \partial/\partial\boldsymbol{r}$ and $\nabla_{m\boldsymbol{L}} = \partial/\partial\boldsymbol{r}_{m\boldsymbol{L}}$ represent, respectively, the gradients with respect to the space position $\boldsymbol{r}$ and with respect to the atom position at $\boldsymbol{r}_m + \boldsymbol{L}$ (that is an image if $\boldsymbol{L} \neq 0$); $\hat{v}_0$ represents the (possibly non-local) ionic (pseudo-) potential acting on the electrons; LDA and GGA indicate the local-density [46] and generalized-gradient [36] approximations for the XC energy functional and $\partial\epsilon^{\text{GGA}}$ is the derivative of the GGA XC local energy per particle with respect to density gradients. All the terms in Eq. (8) are well defined under periodic boundary conditions (PBC) [13]. Only the expression of $\boldsymbol{J}^{KS}$ depends on the choice of the arbitrary zero of the one-electron energy levels. A shift of this zero by $\Delta\epsilon$ results in a KS energy flux shifted by $\Delta\epsilon\boldsymbol{J}^\rho$, $\boldsymbol{J}^\rho$ being the adiabatic electronic flux [47], $\boldsymbol{J}^\rho = 2\sum_v\langle\dot{\varphi}_v|\hat{\boldsymbol{r}}|\varphi_v\rangle$ (the factor 2 accounts for spin degeneracy in a singlet state), which is also well defined within PBC. The adiabatic electronic flux is non-diffusive, being the difference between the total-charge flux, which is by definition non-diffusive in insulators [48], and its ionic component, non-diffusive in mono-atomic and molecular systems, because of momentum conservation and the condition that molecular bonds do not break [13, 16]. Therefore, $\boldsymbol{J}^\rho$ does not contribute to the heat conductivity, thus lifting this further apparent indeterminacy of the transport coefficient derived from the MUB energy flux.

III. DEEP POTENTIAL MODEL

To speed up equilibrium MD simulations, we trained a DNN model according to the DP framework [23]. Consider a system of N atoms, whose configurations are represented by the set of atomic positions, $\boldsymbol{r} = \{\boldsymbol{r}_1, \boldsymbol{r}_2, \ldots, \boldsymbol{r}_N\} \in \mathbb{R}^{3N}$. For each atom, n, we consider only the neighbours, $\{q\}$, such that $r_{qn} < r_c$, where r_{qn} is the modulus of the vector $\boldsymbol{r}_{qn} = [x_{qn}, y_{qn}, z_{qn}] \doteq \boldsymbol{r}_q - \boldsymbol{r}_n$, and r_c is a pre-defined cut-off radius. Denoting with N_n the number of neighbours of n within the cutoff radius, we define the *local environment matrices* $\tilde{R}_n \in \mathbb{R}^{N_n \times 4}$ to encode the local environment:

$$\tilde{R}_n = \begin{bmatrix} \frac{\sigma(r_{1n})}{r_{1n}} & \frac{\sigma(r_{1n})x_{1n}}{r_{1n}^2} & \frac{\sigma(r_{1n})y_{1n}}{r_{1n}^2} & \frac{\sigma(r_{1n})z_{1n}}{r_{1n}^2} \\ \frac{\sigma(r_{2n})}{r_{2n}} & \frac{\sigma(r_{2n})x_{2n}}{r_{2n}^2} & \frac{\sigma(r_{2n})y_{2n}}{r_{2n}^2} & \frac{\sigma(r_{2n})z_{2n}}{r_{2n}^2} \\ \vdots & \vdots & \vdots & \vdots \end{bmatrix}, \quad (10)$$

where $\sigma(r_{qn})$ is a smoothing function (see Appendix A). Then, symmetry-preserving descriptors (extensive details in [23]) are constructed and fed to the DNN, which returns the local energy contribution w_n in output. We denote by $\boldsymbol{W}$ the full set of parameters that define the total potential energy, E. Thus, as illustrated in Ref. 23, the extensive property of E is ensured by its decomposi-

tion into "atomic contributions":

$$E^{\boldsymbol{W}}(\{\tilde{R}\}) = \sum_n w^{\boldsymbol{W}_{\alpha_n}}(\tilde{R}_n) \equiv \sum_n w_n \qquad (11)$$

where α_n denotes the chemical species of atom n. We use the notation $(\dots)^{\boldsymbol{W}_{\alpha_n}}$ to indicate that the parameters used to represent the "atomic energy", w_n, only depend on the chemical species α_n of the n-th atom. Being w_n a well defined and easy to compute function of the atomic positions, the atomic forces and their breakup into individual atomic contributions, $\frac{\partial w_m}{\partial \boldsymbol{r}_n}$ (needed in the definition of the energy flux in Eq. (1)), can be easily computed as the gradients of E and w_n, respectively. In particular, the computation of the latter can be divided into two contributions by applying the chain rule:

$$\nabla_{\boldsymbol{r}_n} w_m = \frac{\partial w_m}{\partial \boldsymbol{r}_n} = \sum_{i,j} \frac{\partial w_m}{\partial \tilde{R}_m^{ij}} \frac{\partial \tilde{R}_m^{ij}}{\partial \boldsymbol{r}_n} \qquad (12)$$

where i,j identifies an element of the matrix $\tilde{R}_m$. The first terms can be easily computed with TensorFlow [49], while the second must be handled separately and coded explicitly [21, 23]. A more detailed description of the calculation can be found in Appendix A. The local energy and its derivatives are the key elements in the computation of the energy flux, Eq. (2). The parameters of the model are determined by minimizing the loss function:

$$L = p_E \Delta E^2 + \frac{p_f}{3N} \sum_n \Delta \boldsymbol{F}_n^2 \qquad (13)$$

where ΔE^2 and $\Delta \boldsymbol{F}_n^2$ are the squared deviations of the potential energy and atomic forces, respectively, between the reference DFT model and the DNN predictions. The two prefactors, p_E and p_f, are needed to optimize the training efficiency and to account for the difference in the physical dimensions of energies and forces.

We remark that gauge invariance is instrumental in ensuring the uniqueness of the heat conductivity in a DNN framework. In fact, the roughness of the loss-function landscape implies that equally good representations of the potential-energy surface and atomic forces may be reached with very different representations of the atomic contributions to the total energy. Gauge invariance implies that, if the total energies resulting from two different local representations were identical, the resulting transport coefficients would also be identical, thus making them in practice dependent on the overall accuracy of the DNN model, but not on the details of its local representation.

IV. RESULTS

A. Ab initio Molecular Dynamics

We performed four *ab initio* MD simulations of water, corresponding to different temperatures and phases, using the PBE functional approximation of DFT, the plane-wave pseudopotential method, and periodic boundary conditions. Hamann-Schlüter-Chiang-Vanderbilt (HSCV) norm-conserving pseudopotentials [50] were used with a kinetic-energy cutoff of 85 Ry. All the simulations were performed with the Car-Parrinello extended-Langrangian method [51] using the cp.x component of QUANTUM ESPRESSO™ [52–54] and setting the fictitious electronic mass to 25 physical masses and the timestep to $dt = 0.073$ fs. Liquid water simulations were done with 125 water molecules inside a cubic computational box of side $l = 15.52$ Å, hexagonal ice-Ih simulations used 128 water molecules inside an orthogonal cell, with sides: $l_1 = 18.084$ Å, $l_2 = 15.664$ Å and $l_3 = 14.724$ Å. It is known that within the PBE XC functional approximation, liquid water exhibits enhanced short-range order [55, 56] and a melting temperature that is more than 100 K higher than in experiment [39, 57], while solid ice has higher density than liquid water at coexistence. In order to compensate for this shortfall, it is customary to offset the simulation conditions by increasing the temperature by ≈ 100 K. We performed simulations of the liquid at three temperatures (521 K, 431 K and 409 K), and of ice in the hexagonal Ih structure at 260 K. Each simulation was 100 ps long. Then, using the QEHeat [17] code, we computed the MUB flux every 3.1 fs. The statistical noise affecting the estimates of the GK integrals is larger when the spectral power of the flux time series is larger. Because of gauge invariance, different representations of the energy current may carry a very different spectral power, and still yield the same conductivity, which is the zero-frequency limit of the flux power spectrum. The MUB energy flux turns out to carry an impractically large spectral power, which can be tamed to some extent by leveraging gauge and convective invariance. Gauge invariance is first exploited by the *velocity renormalization* technique of Ref. 45. In a nutshell, it can be demonstrated that subtracting to each atomic velocity the average velocity of all the atoms of the same chemical species, results in a current with a much reduced spectral weight but the same conductivity. Further spectral weight can be subtracted by adding to the resulting effective flux any linear combination of non-diffusive fluxes. This can be effectively done by treating the (possibly renormalized) energy current as one component of an M-component system, where all the other currents are non-diffusive ones [16]. Here, we choose $M = 2$ and take the electronic adiabatic current as the auxiliary non-diffusive one. In all cases, the transport coefficients are obtained from the *cepstral analysis* [15, 16] of the power spectrum of the relevant currents, using the SporTran [58] code.

Fig. 1 displays the (window-filtered) power spectrum of the MUB flux from one of our Car-Parrinello MD simulations of liquid water at an average temperature of 431 K, using renormalized velocities (orange line), and further removing the contribution of the adiabatic electron current from the energy flux (blue line). In the inset we see
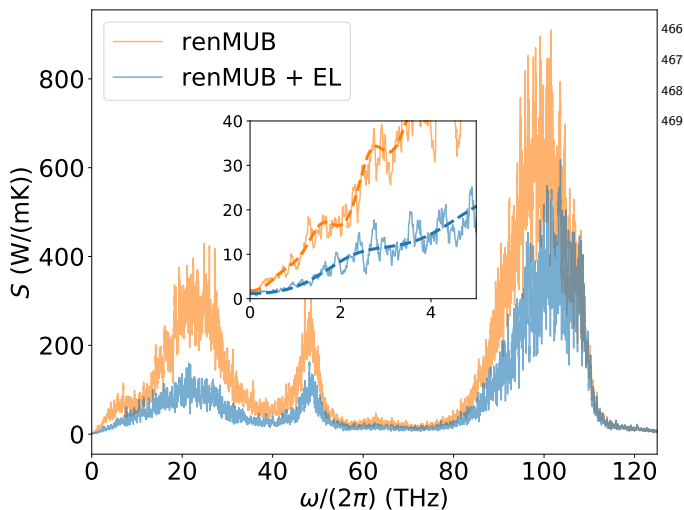
FIG. 1. Comparison of the (window-filtered) spectrum of the velocity renormalized MUB flux (orange) and of the velocity renormalized MUB flux decorrelated with the adiabatic electronic flux (blue). Both spectrum are filtered with a moving average of 0.1 THz. The renormalized MUB flux has a higher power but close to zero the two spectra converge to the same value. The two dashed lines in the inset represent the cepstral filters of the power spectra.

that the two spectra converge to the same value when $\omega = 0$. The decorrelation decreases the power of the spectrum and flattens the spectrum near $\omega = 0$ facilitating data analysis by reducing the number of the required cepstral coefficients.

B. DPMD benchmark against GGA results

In order to appraise the ability of DP models to accurately describe heat transport phenomena, we have generated one such model, by training it on a set of DFT-PBE data extracted from Car-Parrinello trajectories at different temperatures in the [400K – 1000K] temperature range. The loss function in Eq. (13) was optimized with the Adam stochastic gradient descent method [59]. The details of the training protocol are given in Appendix B. The generated DNN potential was then used to run equilibrium MD simulations of water at the same conditions explored in the previous subsection by *ab initio* techniques. One of the resulting energy-flux power spectra is displayed in Fig. 2 (orange), together with the corresponding *ab initio* spectrum (blue). The thermal conductivities corresponding to the two spectra are obtained as before through cepstral analysis. Notice that, in spite of the much larger weight of the *ab initio* spectrum relative to that of the DNN model, the two spectra have the same low-frequency limit, indicating that the two simulations predict the same conductivity within statistical errors. The difference between the two spectra stems much more from the different local representations

of the potential energy than from a different dynamics. The latter is, in fact, very well mimicked by the DNN potential, which gives forces in close agreement with those of the *ab initio* model (see Appendix B 3).
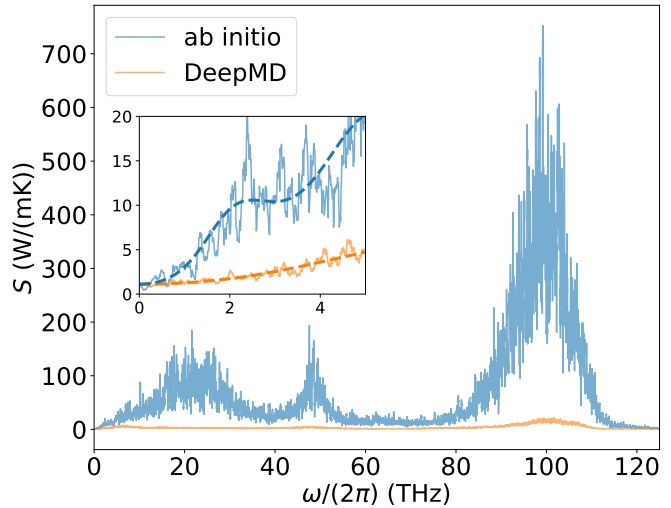
FIG. 2. Power spectrum of a water simulation. The orange line is obtained from 360 ps of DPMD simulation of a periodic cubic cell containing 125 water molecules at 407 K. The blue line is obtained from an *ab initio* MD simulation of 125 water molecules with the same cubic box and an average temperature of 409 K. Both spectrum are filtered with a moving average of 0.1 THz. The dashed lines in the inset represent the cepstral-filtered spectra. Even though the two spectra have very different intensities the values at zero frequency are the same.

In Table I we display the thermal conductivities computed from *ab initio* MD and DPMD for all the simulations that we performed, together with the atomic diffusivities, D_H and D_O. The latter are computed from the $\omega = 0$ value of the power spectrum of the velocity:

$$\bar{D}_\alpha(\omega) = \frac{1}{6N_\alpha} \sum_n^{N_\alpha} \int_{-\infty}^{\infty} \langle \boldsymbol{v}_n(0) \cdot \boldsymbol{v}_n(t) \rangle \, e^{i\omega t} dt \qquad (14)$$

where α represents the atomic species (oxygen and hydrogen here) and n runs over all the atoms of species α. The diffusivities are obtained from a block analysis of a 100 ps long trajectory. The DP model was capable of reproducing accurately the three transport coefficients. In particular, it allowed us to perform longer simulations in order to reduce the statistical uncertainty on κ. While ≈ 100 ps long trajectories suffice for errors of about 10% in liquid water and of about 20% in ice Ih, we found that ≈ 360 ps long trajectories with the DP model reduced these errors to 5% and 8%, respectively. These errors could be reduced even further because trajectories lasting tens of ns or more would be possible with DPMD.

The calculated heat conductivities with DPMD and *ab initio* MD, based on PBE-DFT, agree closely among them, but differ substantially from experiment ($\kappa_{expt} \approx$

| | phase | T | D_H | D_O | κ |
		K	Å^2/ps	Å^2/ps	W/(mK)
DPMD	liquid	516	1.07 ± 0.05	1.08 ± 0.05	0.99 ± 0.05
	liquid	423	0.41 ± 0.02	0.42 ± 0.02	1.03 ± 0.05
	liquid	408	0.29 ± 0.02	0.32 ± 0.02	1.11 ± 0.05
	ice Ih	270	-	-	1.9 ± 0.2
ab initio	liquid	521	1.13 ± 0.05	1.11 ± 0.05	0.98 ± 0.19
	liquid	431	0.45 ± 0.03	0.45 ± 0.03	1.06 ± 0.11
	liquid	409	0.325 ± 0.018	0.29 ± 0.02	1.12 ± 0.17
	ice Ih	260	-	-	1.8 ± 0.4

TABLE I. Comparison of some properties of water from *ab initio* MD and DPMD simulations based on PBE-DFT. All liquid simulations used 125 H_2O molecules inside a cubic box of side $l = 15.52$ Å. The ice Ih simulations used 128 H_2O molecules inside an orthogonal cell with sides: $l_1 = 18.084$ Å, $l_2 = 15.664$ Å and $l_3 = 14.724$ Å. T is the mean temperature of the simulations; D_H and D_O are the diffusivities of hydrogen and oxygen, respectively; while κ is the thermal transport coefficient. The diffusivities of ice Ih are compatible with zero and are not reported.

0.6 W/(mK) *vs.* $\kappa_{PBE} \approx 1$ W/(mK) for water at near ambient conditions [60]), indicating that the distribution of the energy density resulting from the PBE functional adopted here is likely inadequate to accurately describe adiabatic energy transport in water. This prompted us to try more advanced functional approximations, like the meta-GGA SCAN framework, to cope with this shortcoming.

V. EXTENDED SIMULATIONS WITH A SCAN BASED DEEP POTENTIAL MODEL

Meta-GGA functionals like SCAN depend on the electronic kinetic energy density, in addition to the density and its gradient, making significantly more complicated than in the PBE case the derivation of an analytic expression for the energy flux to use in *ab initio* MD studies of heat transport. However, this is not necessary, as the DPMD methodology not only gives us a framework for molecular simulations having quantum-mechanical accuracy at a cost close to that of empirical force fields, but also offers us the capability of easily deriving a practical expression for the energy flux, in situations where it would be difficult to obtain it directly from first principles. To follow this route, we trained a DP model using the SCAN-DFT dataset of Ref. 61. The thermal conductivity predicted by this model, at $T \approx 430$ K and at the same density used in our previous PBE simulations, is $\kappa = 0.88 \pm 0.05$W/(mK), which is closer to experiment, but still not in perfect agreement with it. Recent studies [24, 62] found that the melting temperature of SCAN-DP ice Ih models is around 310 K, a value very close to the corresponding DFT temperature, according to perturbative estimates [62]. While still not perfect, this result is far superior to PBE, whose estimated ice Ih melting temperature should be around 400 K or higher [39, 57]. Thus, one might argue that the 100 K temperature offset used in our PBE-DFT simulations would be inappropriate here, but the rather broad temperature range displayed in Fig. 3 shows that the thermal conductivity of water is rather insensitive to temperature at near ambient pressure.

The simulations reported in Fig. 3 have been performed by fixing the size of the simulation-box in order to match the experimental density [63] at each reported temperature. At each temperature, we first performed an NVT simulation lasting for a few dozen ps, in which the system was coupled to a Nosé-Hoover thermostat, followed by a 880 ps long NVE simulation, in order to compute the thermal transport coefficient. The solid line in Fig. 3 connects PBE data at temperatures below 400 K, i.e., below the estimated freezing temperature of this model [39, 57]. At these temperatures PBE water is sluggish and difficult to equilibrate.

SCAN overestimates κ less than PBE, consistent with the better representation of the covalent bond length of the water molecule in the liquid provided by this functional [38]. The experimental data show a broad maximum around 400 K, while PBE exhibits a sharp maximum around 360 K, i.e., below the estimated freezing point of this model. The SCAN results are closer to experiment and are consistent with a broad maximum of the thermal conductivity in the explored region. Whether the residual discrepancy between DFT-SCAN simulations and experiment is due to a residual inaccuracy of the XC functional or to neglect of quantum effects on the nuclear motion is an issue that would require further work to be clarified.

VI. CONCLUSIONS

In this work we have shown that DNN potentials generated according to the DP framework and properly trained on DFT data are a powerful tool to study the transport properties of water, and likely of other material systems, with quantum-mechanical accuracy at a nearly empirical force field cost. An important byproduct of this technology is that it allows one to derive numerically practical expressions for the energy current, even in cases where analytical derivations from the DFT functional would be hard, as we have shown in the case of the SCAN functional. Our results show that PBE-DFT overestimates
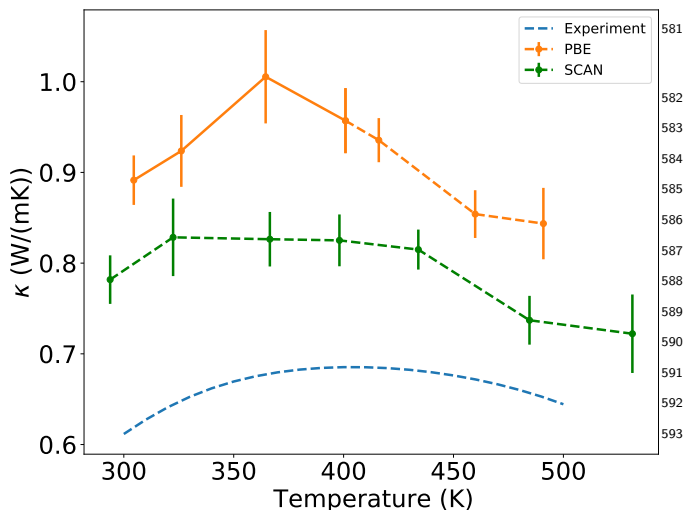
FIG. 3. Temperature dependence of the thermal conductivity κ of water between 300 K and 500 K. The blue line represents the experimental data from the NIST website [63]. The orange and green lines result from (classical) DPMD simulations trained on PBE and SCAN data, respectively. The simulations use a periodically repeated cubic box with 128 water molecules. In the simulations the box size is fixed to the experimental density [63] at each given temperature. Relative to PBE, SCAN overestimates less the experimental values, and varies less with temperature, consistent with experiment. PBE exhibits a relatively sharp conductivity maximum at around 360 K, whereas experiment shows a broad maximum at ≈ 400 K. The sharp PBE maximum may be an artifact of imperfect equilibration in a metastable liquid. The continuous line connects data points below the freezing temperature at ≈ 400 K, where the PBE liquid is metastable. In the Supplementary Material [64] the reader can find the files containing the data points for the DPMD-PBE and DPMD-SCAN simulations shown in the figure

.

the thermal conductivity by $\approx 60\%$. The SCAN meta-GGA functional reduces this error by approximately a factor of two, which is not quite negligible. Whether this residual discrepancy should be ascribed mostly to residual inaccuracies of the XC energy functional or to neglect of nuclear quantum effects in the particle dynamics, is an issue that deserves further study. As a final remark, we would like to stress that the method presented here should be useful in fields, such as, e.g., the geosciences and the planetary sciences, where the transport properties of different phases of matter at extreme pressure and temperature conditions, that are difficult to reproduce in the laboratory, are a key ingredient in quantitative evolutionary models of the earth and/or other planets. The reliability of such models stands in fact on the accuracy of the relevant conductivities under the thermodynamic conditions of interest [65, 66].

DATA AND CODE AVAILABILITY

In the Supplementary Material [64] the reader can find two files, `kappa_T_DPMD-PBE.dat` and `kappa_T_DPMD-SCAN.dat`, containing the data points shown in Fig. 3 for the DPMD-PBE and DPMD-SCAN simulations, respectively.

In the latest versions of DeePMD-kit the authors released a code to compute the heat current with the method presented in this paper. This code extends the LAMMPS [67–69] interface of DeePMD-kit allowing the computation of the heat current via the command `compute heat/flux`. For more info see the documentation on DeePMD-kit [70].

Appendix A: Derivatives

The derivative of the local energy, $\frac{\partial w_m}{\partial \boldsymbol{r}_n}$, is a key component in the computation of the energy flux, Eq. (2). As already mentioned in Section III, it is composed of two terms, i.e., $\frac{\partial w_m}{\partial \tilde{R}_m}$ and $\frac{\partial \tilde{R}_m}{\partial \boldsymbol{r}_n}$. Since w_n is a well defined and easy to compute function of the *local environment matrices* $\tilde{R}_m$ [23], the first term can be easily obtained from TensorFlow [49] using the same back-propagation approach that is commonly used during the training of a DNN [71, 72]. The second term must, instead, be computed explicitly [21, 23]. Given the definition in Eq. (10) and the following smoothing function:

$$\sigma(r_{mn}) = \begin{cases} 1 & r_{mn} < r_{c1} \\ -6\Omega^5 + 15\Omega^4 - 10\Omega^3 + 1 & r_{c1} < r_{mn} < r_c \\ 0 & r_c < r_{mn} \end{cases}$$
(A1)

where r_{c1} is the smoothing cut-off radius and $\Omega = \frac{r_{mn}-r_{c1}}{r_c-r_{c1}}$, we get by applying the chain rule:

$$\frac{\partial \tilde{R}_m}{\partial r_n^\tau} = \frac{\partial \tilde{R}_m}{\partial r_{ql}^\gamma} \frac{\partial r_{ql}^\gamma}{\partial r_n^\tau}$$
(A2)

where sums on repeated indices are implied, and $\tau, \gamma = 1, 2, 3 \equiv x, y, z$ denote Cartesian coordinates. We find:

$$\frac{\partial r_{ql}^{\gamma}}{\partial r_n^{\tau}} = \delta_{\gamma,\tau}(\delta_{n,q} - \delta_{n,l}) \qquad (A3)$$

$$\frac{\partial \tilde{R}_m}{\partial r_{ql}^{\gamma}} = \frac{\partial \tilde{R}_m}{\partial r_{qm}^{\gamma}}\delta_{l,m} + \frac{\partial \tilde{R}_m}{\partial r_{ml}^{\gamma}}\delta_{q,m} \qquad (A4)$$

where δ_{nm} is the Kronecker delta.

Using i, j to represent line and column indices of the element of $\tilde{R}_m$ to be differentiated, a general element of $\left[\frac{\partial \tilde{R}_m}{\partial r_{qm}^{\gamma}}\right]_{ij}$ is non-zero only if atom q is the $i-th$ neighbour of m in the matrix $\tilde{R}_m$:

$$\left[\frac{\partial \tilde{R}_m}{\partial r_{qm}^{\gamma}}\right]_{i,j} = \begin{cases} \frac{r_{qm}^{\gamma}}{r_{qm}^2}\left(\frac{\partial \sigma_{qm}}{\partial r_{qm}} - \frac{\sigma_{qm}}{r_{qm}}\right) & \text{if } j = 1 \\ \frac{\partial \sigma_{qm}}{\partial r_{qm}}\frac{r_{qm}^{\gamma} r_{qm}^{j-1}}{r_{qm}^3} - 2\sigma\frac{r_{qm}^{\gamma} r_{qm}^{j-1}}{r_{qm}^4} \\ + \delta_{\gamma,j-1}\frac{\sigma_{qm}}{r_{qm}^2} & \text{if } j \neq 1 \end{cases} \qquad (A5)$$

where $\sigma_{nm} = \sigma(r_{nm})$. With the same approach a similar expression for $\left[\frac{\partial \tilde{R}_m}{\partial r_{ml}^{\gamma}}\right]_{i,j}$ can be obtained.

Appendix B: Neural network training

1. Training parameters

The NN PBE model in Section IV B is constructed with the DeePMD-kit [73] and the present appendix contains the main parameters of the model. In the definition of the *local environment matrices*, the two radii inside the smoothing function in Eq. (A1) are $r_{c1} = 3.50$ Åand $r_c = 7.00$ Å. The embedding network has three layers with 25, 50 and 100 neurons respectively, whereas the fitting network has three layers with 240 neurons each. The loss function is optimized using the Adam stochastic gradient descent method [59], with a learning rate starting at 0.005 and exponentially decaying, with a decay rate of 0.98, every 10^5 training step for a total of $1.5 \cdot 10^6$ training steps. In order to optimize training the coefficients p_E and p_f in Eq. (13) were adjusted, respectively, from 0.05 to 1, and from 1000 to 1, during training.

2. Training test

The PBE neural network was tested against a set of $N_v = 800$ independent snapshots of 125 molecules of water at temperatures in the range $[400\text{ K} - 1000\text{K}]$, obtaining a root-mean-square error of the forces of 0.05 eV/Å. Fig. 4 shows a direct comparison between the α component of the *ab initio* force for the s-th atoms in the b-th snapshot and the corresponding NN prediction. The red dashed line correspond to $F_{b,s,\alpha}^{\text{NN}} = F_{b,s,\alpha}^{\text{DFT}}$, that fits the data with a *coefficient of determination* $R^2 = 0.998$. R^2 is computed with the usual formula for linear regression:

$$R^2 = 1 - \frac{\sum_i (F_i^{\text{DFT}} - F_i^{NN})^2}{\sum_i (F_i^{\text{DFT}} - \bar{F}^{DFT})^2}, \qquad (B1)$$

where $\bar{F}^{DFT}$ is the average of all the force components in the dataset.
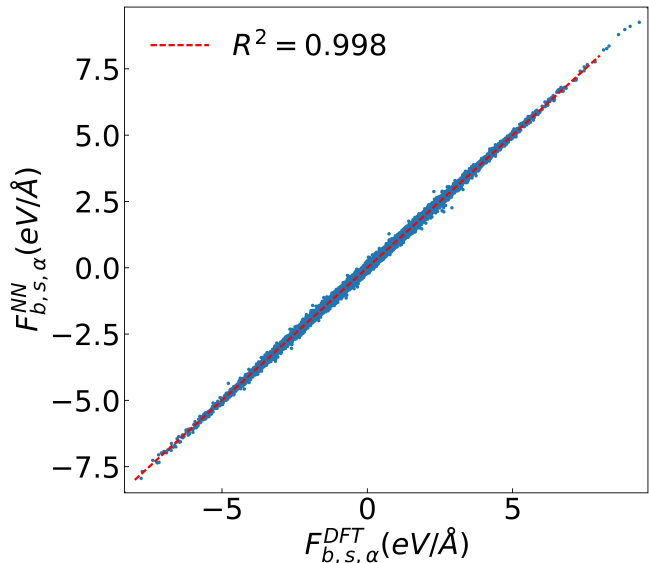

FIG. 4. Direct comparison between the *ab initio* force components and the corresponding NN prediction. The indexes b, s, α (see main text) label, respectively, the snapshot, the atom, and the Cartesian coordinate of the force. The red dashed line represent $F_{b,s,\alpha}^{\text{DFT}} = F_{b,s,\alpha}^{\text{NN}}$, that fits the data with $R^2 = 0.998$.

3. Benchmark of water properties

To estimate the quality of the trained DP model we compared some simple static and dynamical properties of the model with their *ab initio* counterparts. We ran DPMD simulations of water at the same thermodynamic conditions of the *ab initio* simulations reported in Section IV A. Figs. 5 and 6 compares the oxygen radial distribution functions, $g(r)$, from DP and *ab initio* simulations of liquid water (third and seventh line of Table I), and of ice-Ih (fourth and last line of Table I). Both structures are well described by the DP model. This is true also for the ice-structure even though no ice-snapshots were included in the training data set.

For liquid water, we computed also the power spectra of the oxygen and hydrogen velocities Eq. (14), respectively, and their zero frequency values, the diffusion coefficients. Fig. 7 shows the power spectra of liquid water systems mentioned above. It can be seen that DP and *ab initio* models give consistent diffusivities (see Table I for a complete comparison of the results): $D_H^{\text{AIMD}} =$

0.325 ± 0.018 Å^2/ps, $D_H^{\mathrm{NN}} = 0.29 \pm 0.02$ Å^2/ps, $D_O^{\mathrm{AIMD}} = 0.29 \pm 0.02$ Å^2/ps and $D_O^{\mathrm{NN}} = 0.32 \pm 0.02$ Å^2/ps.
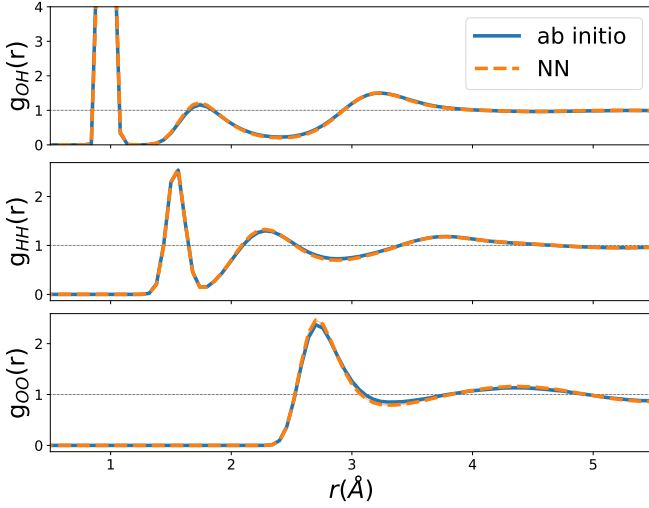

FIG. 5. Comparison of the radial distribution functions of liquid water from *ab initio* (continuous blue line) and DP (dashed orange line) simulations, respectively. More details on the simulations can be found in the main text.
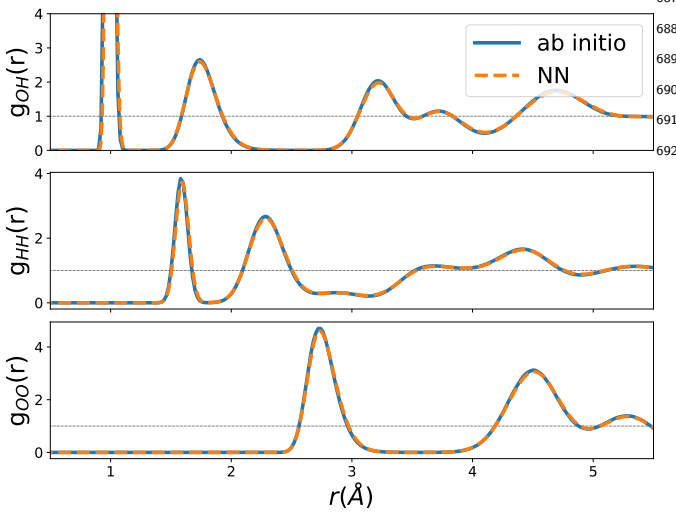

FIG. 6. Comparison of the radial distribution functions of ice Ih from *ab initio* (continuous blue line) and DP (dashed orange line) simulations, respectively. More details on the simulations can be found in the main text.

Appendix C: Cepstral analysis of the flux time series

In the present work the thermal conductivity is computed via the cepstral analysis of the energy flux, as implemented in the `SporTran` code [58]. This technique provides a very accurate and reliable estimate of the transport coefficients and their statistical accuracy, depending only on two parameters: the effective Nyquist frequency,
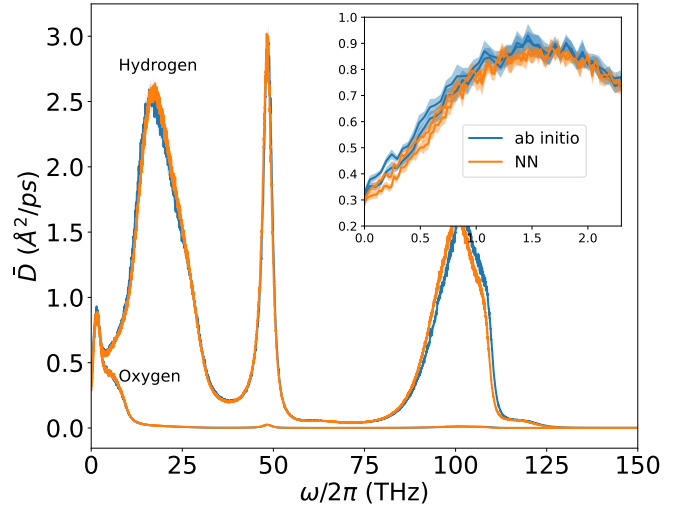

FIG. 7. Comparison of the oxygen and hydrogen velocity power spectra of liquid water from *ab initio* (blue line) and DP (orange line) simulations, respectively. The simulations used the same periodic cubic cell with density $\rho = 1.00$ g/cm^3 containing 125 water molecules, at $\approx 410K$. The inset shows the region near $\omega = 0$ used to estimate the diffusivity.

f^*, used to limit the analysis to a properly defined low-frequency window, and the number P^* of cepstral coefficients. For a detailed explanation of the method and the meaning of the parameters the reader may consult [15, 42, 44]. Table II contains the parameters used to obtain the values of κ in Table I.

	phase	T K	f^* THz	P^*
DPMD	liquid	516	9.9	11
	liquid	423	17.8	12
	liquid	408	36.7	17
	ice Ih	270	25	93
ab initio	liquid	521	20.7	55
	liquid	431	20.1	17
	liquid	409	45.9	33
	ice Ih	260	30.3	53

TABLE II. Table with the value of f^* and P^* used to obtained the values in Table I.

Appendix D: Size scaling for SCAN neural network potential

Size effects may affect the transport properties calculated in numerical simulations [74, 75]. In order to quantify these effects, we run 2 ns long NVE simulations at ≈ 407 K of SCAN-DP water at fixed density and increasingly larger cells (with up to 1000 molecules). The results, reported in Fig. 8, suggest that κ shows no size dependence within the error bars of the simulation.
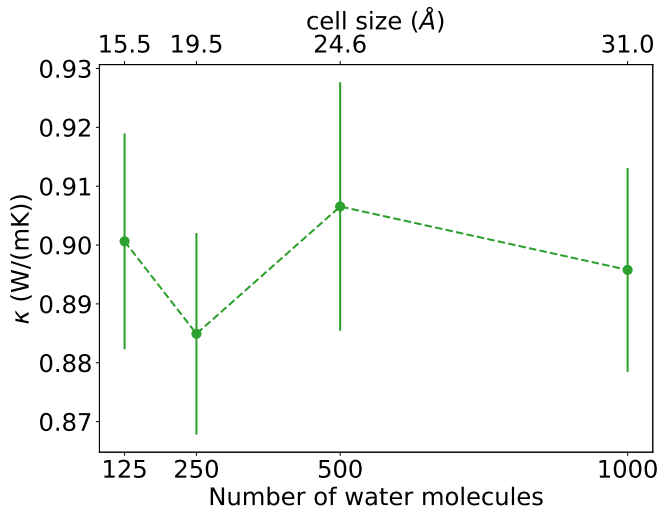
FIG. 8. The size dependence of the thermal transport coefficient κ for simulation with the SCAN neural network potential. The test shows that no relevant size scale dependence is observed. All the quantities are evaluated from $\approx$ 2ns long trajectories.

[1] R. Peierls, Zur kinetischen theorie der wärmeleitung in kristallen, Annalen der Physik **395**, 1055 (1929), translated in: R. E. Peierls, *On the Kinetic Theory of Thermal Conduction in Crystals*, in R. H. Dalitz and R. E. Peierls (ed.), Selected Scientific Papers of Sir Rudolf Peierls with Commentary, vol. 19, World Scientific Publishing Co., Singapore, 1997.

[2] P. Klemens, Thermal Conductivity and Lattice Vibrational Modes, in *Solid State Physics - Advances in Research and Applications*, Vol. 7 (1958) pp. 1–98.

[3] D. A. Broido, M. Malorny, G. Birner, N. Mingo, and D. A. Stewart, Intrinsic lattice thermal conductivity of semiconductors from first principles, Applied Physics Letters **91**, 231922 (2007).

[4] F. Zhou, W. Nielson, Y. Xia, and V. Ozoliņš, Lattice anharmonicity and thermal conductivity from compressive sensing of first-principles calculations, Physical Review Letters **113**, 185501 (2014), arXiv:1404.5923.

[5] D. J. Evans and G. P. Morriss, *Statistical Mechanics of Nonequilibrium Liquids* (2007).

[6] M. P. Allen and D. J. Tildesley, *Mathematics of Computation*, Vol. 1 (Oxford University Press, 2017) p. 442.

[7] F. Müller-Plathe, A simple nonequilibrium molecular dynamics method for calculating the thermal conductivity, The Journal of Chemical Physics **106**, 6082 (1997).

[8] A. Tenenbaum, G. Ciccotti, and R. Gallico, Stationary nonequilibrium states by molecular dynamics. Fourier's law, Physical Review A **25**, 2778 (1982).

[9] M. S. Green, Markoff random processes and the statistical mechanics of time-dependent phenomena, ii. irreversible processes in fluids, J. Chem. Phys. **22**, 398–413 (1954).

[10] R. Kubo, Statistical-mechanical theory of irreversible processes. i. general theory and simple applications to magnetic and conduction problems, J. Phys. Soc. Jpn. **12**, 570 (1957).

[11] J. Kang and L.-W. Wang, First-principles Green-Kubo method for thermal conductivity calculations, Physical Review B **96**, 020302(R) (2017).

[12] C. Carbogno, R. Ramprasad, and M. Scheffler, Ab initio Green-Kubo approach for the thermal conductivity of solids, Phys. Rev. Lett. **118**, 175901 (2017).

[13] A. Marcolongo, P. Umari, and S. Baroni, Microscopic theory and quantum simulation of atomic heat transport, Nature Physics **12**, 80 (2016).

[14] L. Ercole, A. Marcolongo, P. Umari, and S. Baroni, Gauge Invariance of Thermal Transport Coefficients, JLTP **185**, 79 (2016).

[15] L. Ercole, A. Marcolongo, and S. Baroni, Accurate thermal conductivities from optimally short molecular dynamics simulations, Scientific Reports **7**, 15835 (2017).

[16] R. Bertossa, F. Grasselli, L. Ercole, and S. Baroni, Theory and Numerical Simulation of Heat Transport in Multicomponent Systems, Physical Review Letters **122**, 255901 (2019), arXiv:1808.03341.

[17] A. Marcolongo, R. Bertossa, D. Tisi, and S. Baroni, QE-Heat: an open-source energy flux calculator for the computation of heat-transport coefficients from first principles, Computer Physics Communications **269**, 108090 (2021).

[18] J. Behler and M. Parrinello, Generalized Neural-Network Representation of High-Dimensional Potential-Energy Surfaces, Physical Review Letters **98**, 146401 (2007).

[19] R. Kondor, N-body networks: a covariant hierarchical neural network architecture for learning atomic potentials (2018), arXiv:1803.01588.

[20] J. S. Smith, O. Isayev, and A. E. Roitberg, ANI-1: an extensible neural network potential with DFT accuracy at force field computational cost, Chemical Science 8, 3192 (2017), arXiv:1610.08935.

[21] L. Zhang, J. Han, H. Wang, R. Car, and W. E, Deep Potential Molecular Dynamics: A Scalable Model with the Accuracy of Quantum Mechanics, Physical Review Letters 120, 143001 (2018), arXiv:arXiv:1707.09571v1.

[22] A. P. Bartók, M. C. Payne, R. Kondor, and G. Csányi, Gaussian Approximation Potentials: The Accuracy of Quantum Mechanics, without the Electrons, Physical Review Letters 104, 136403 (2010), arXiv:0910.1019.

[23] L. Zhang, J. Han, H. Wang, W. Saidi, R. Car, and W. E, End-to-end symmetry preserving inter-atomic potential energy model for finite and extended systems, in Advances in Neural Information Processing Systems 31, edited by S. Bengio, H. Wallach, H. Larochelle, K. Grauman, N. Cesa-Bianchi, and R. Garnett (Curran Associates, Inc., 2018) pp. 4436–4446.

[24] L. Zhang, H. Wang, R. Car, and W. E, Phase diagram of a deep potential water model, Phys. Rev. Lett. 126, 236001 (2021).

[25] W. Jiang, Y. Zhang, L. Zhang, and H. Wang, Accurate Deep Potential model for the Al–Cu–Mg alloy in the full concentration space*, Chinese Physics B 30, 050706 (2021), arXiv:2008.11795.

[26] C. Zhang, F. Tang, M. Chen, L. Zhang, D. Y. Qiu, J. P. Perdew, M. L. Klein, and X. Wu, Modeling liquid water by climbing up Jacob's ladder in density functional theory facilitated by using deep neural network potentials (2021), arXiv:2104.14410 [physics.chem-ph].

[27] J. Wu, Y. Zhang, L. Zhang, and S. Liu, Deep learning of accurate force field of ferroelectric HfO$_2$, Phys. Rev. B 103, 024108 (2021).

[28] T. E. Gartner, L. Zhang, P. M. Piaggi, R. Car, A. Z. Panagiotopoulos, and P. G. Debenedetti, Signatures of a liquid–liquid transition in an ab initio deep neural network model for water, Proceedings of the National Academy of Sciences 117, 26040 (2020).

[29] H. Niu, L. Bonati, P. M. Piaggi, and M. Parrinello, Ab initio phase diagram and nucleation of gallium, Nature Communications 11, 2654 (2020).

[30] W. Jia, H. Wang, M. Chen, D. Lu, L. Lin, R. Car, W. E, and L. Zhang, Pushing the limit of molecular dynamics with ab initio accuracy to 100 million atoms with machine learning, in Proceedings of the International Conference for High Performance Computing, Networking, Storage and Analysis (IEEE Press, 2020).

[31] A. Marcolongo, T. Binninger, F. Zipoli, and T. Laino, Simulating diffusion properties of solid-state electrolytes via a neural network potential: Performance and training scheme, ChemSystemsChem 2, 10.1002/syst.201900031 (2019), arXiv:1910.10090.

[32] J. Huang, L. Zhang, H. Wang, J. Zhao, J. Cheng, and W. E, Deep potential generation scheme and simulation protocol for the Li10GeP2S12-type superionic conductors, The Journal of Chemical Physics 154, 094703 (2021).

[33] R. Li, E. Lee, and T. Luo, A unified deep neural network potential capable of predicting thermal conductivity of silicon in different phases, Materials Today Physics 12, 100181 (2020).

[34] L. Zhang, M. Chen, X. Wu, H. Wang, W. E, and R. Car, Deep neural network for the dielectric response of insulators, Phys. Rev. B 102, 041121(R) (2020).

[35] G. M. Sommers, M. F. Calegari Andrade, L. Zhang, H. Wang, and R. Car, Raman spectrum and polarizability of liquid water from deep neural networks, Phys. Chem. Chem. Phys. 22, 10592 (2020).

[36] J. P. Perdew, K. Burke, and M. Ernzerhof, Generalized gradient approximation made simple, Phys. Rev. Lett. 77, 3865 (1996).

[37] J. Sun, A. Ruzsinszky, and J. P. Perdew, Strongly constrained and appropriately normed semilocal density functional, Phys. Rev. Lett. 115, 036402 (2015).

[38] M. Chen, H.-Y. Ko, R. C. Remsing, M. F. Calegari Andrade, B. Santra, Z. Sun, A. Selloni, R. Car, M. L. Klein, J. P. Perdew, and X. Wu, Ab initio theory and modeling of water, Proceedings of the National Academy of Sciences 114, 10846 (2017).

[39] P. H.-L. Sit and N. Marzari, Static and dynamical properties of heavy water at ambient conditions from first-principles molecular dynamics, The Journal of Chemical Physics 122, 204510 (2005).

[40] A flux, $\boldsymbol{J}$, is defined as the macroscopic average of a current density, $\boldsymbol{j}(\boldsymbol{r})$: $\boldsymbol{J} = \frac{1}{V}\int_V \boldsymbol{j}(\boldsymbol{r})d\boldsymbol{r}$, where V is the system's volume.

[41] E. Helfand, Transport Coefficients from Dissipation in a Canonical Ensemble, Phys. Rev. 119, 1 (1960).

[42] S. Baroni, R. Bertossa, L. Ercole, F. Grasselli, and A. Marcolongo, Heat transport in insulators from ab initio Green-Kubo theory, in Handbook of Materials Modeling: Applications: Current and Emerging Materials, edited by W. Andreoni and S. Yip (Springer International Publishing, Cham, 2018) pp. 1–36, 1802.08006.

[43] S. Stackhouse, L. Stixrude, and B. B. Karki, Thermal Conductivity of Periclase (MgO) from First Principles, Physical Review Letters 104, 208501 (2010).

[44] F. Grasselli and S. Baroni, Invariance principles in the theory and computation of transport coefficients, European Physical Journal B 10.1140/epjb/s10051-021-00152-5 (2021), 2105.02137.

[45] A. Marcolongo, L. Ercole, and S. Baroni, Gauge Fixing for Heat-Transport Simulations., JCTC 16, 3352 (2020).

[46] W. Kohn and L. J. Sham, Self-consistent equations including exchange and correlation effects, Phys. Rev. 140, A1133 (1965).

[47] D. J. Thouless, Quantization of particle transport, Phys. Rev. B 27, 6083 (1983).

[48] F. Grasselli and S. Baroni, Topological quantization and gauge invariance of charge transport in liquid insulators, Nature Physics 15, 967 (2019).

[49] M. Abadi, A. Agarwal, P. Barham, E. Brevdo, Z. Chen, C. Citro, G. S. Corrado, A. Davis, J. Dean, M. Devin, S. Ghemawat, I. Goodfellow, A. Harp, G. Irving, M. Isard, Y. Jia, R. Jozefowicz, L. Kaiser, M. Kudlur, J. Levenberg, D. Mané, R. Monga, S. Moore, D. Murray, C. Olah, M. Schuster, J. Shlens, B. Steiner, I. Sutskever, K. Talwar, P. Tucker, V. Vanhoucke, V. Vasudevan, F. Viégas, O. Vinyals, P. Warden, M. Wattenberg, M. Wicke, Y. Yu, and X. Zheng, TensorFlow: Large-scale machine learning on heterogeneous systems (2015), software available from tensorflow.org.

[50] D. R. Hamann, Optimized norm-conserving Vanderbilt pseudopotentials, Physical Review B 88, 085117 (2013).

[51] R. Car and M. Parrinello, Unified Approach for Molecular Dynamics and Density-Functional Theory, Phys. Rev. Lett. **55**, 2471 (1985).

[52] P. Giannozzi, S. Baroni, N. Bonini, M. Calandra, R. Car, C. Cavazzoni, D. Ceresoli, G. L. Chiarotti, M. Cococcioni, I. Dabo, A. D. Corso, S. de Gironcoli, S. Fabris, G. Fratesi, R. Gebauer, U. Gerstmann, C. Gougoussis, A. Kokalj, M. Lazzeri, L. Martin-Samos, N. Marzari, F. Mauri, R. Mazzarello, S. Paolini, A. Pasquarello, L. Paulatto, C. Sbraccia, S. Scandolo, G. Sclauzero, A. P. Seitsonen, A. Smogunov, P. Umari, and R. M. Wentzcovitch, QUANTUM ESPRESSO: a modular and open-source software project for quantum simulations of materials, Journal of Physics: Condensed Matter **21**, 395502 (2009).

[53] P. Giannozzi, O. Andreussi, T. Brumme, O. Bunau, M. B. Nardelli, M. Calandra, R. Car, C. Cavazzoni, D. Ceresoli, M. Cococcioni, N. Colonna, I. Carnimeo, A. D. Corso, S. de Gironcoli, P. Delugas, R. A. DiStasio, A. Ferretti, A. Floris, G. Fratesi, G. Fugallo, R. Gebauer, U. Gerstmann, F. Giustino, T. Gorni, J. Jia, M. Kawamura, H.-Y. Ko, A. Kokalj, E. Küçükbenli, M. Lazzeri, M. Marsili, N. Marzari, F. Mauri, N. L. Nguyen, H.-V. Nguyen, A. O. de-la Roza, L. Paulatto, S. Poncé, D. Rocca, R. Sabatini, B. Santra, M. Schlipf, A. P. Seitsonen, A. Smogunov, I. Timrov, T. Thonhauser, P. Umari, N. Vast, X. Wu, and S. Baroni, Advanced capabilities for materials modelling with quantum ESPRESSO, Journal of Physics: Condensed Matter **29**, 465901 (2017).

[54] P. Giannozzi, O. Baseggio, P. Bonfà, D. Brunato, R. Car, I. Carnimeo, C. Cavazzoni, S. de Gironcoli, P. Delugas, F. Ferrari Ruffino, A. Ferretti, N. Marzari, I. Timrov, A. Urru, and S. Baroni, Quantum espresso toward the exascale, The Journal of Chemical Physics **152**, 154105 (2020), https://doi.org/10.1063/5.0005082.

[55] J. C. Grossman, E. Schwegler, E. W. Draeger, F. Gygi, and G. Galli, Towards an assessment of the accuracy of density functional theory for first principles simulations of water, The Journal of Chemical Physics **120**, 300 (2004).

[56] E. Schwegler, J. C. Grossman, F. Gygi, and G. Galli, Towards an assessment of the accuracy of density functional theory for first principles simulations of water. II, Journal of Chemical Physics **121**, 5400 (2004), arXiv:0405561.

[57] S. Yoo, X. C. Zeng, and S. S. Xantheas, On the phase diagram of water with density functional theory potentials: The melting temperature of ice Ih with the Perdew–Burke–Ernzerhof and Becke–Lee–Yang–Parr functionals, The Journal of Chemical Physics **130**, 221102 (2009), https://doi.org/10.1063/1.3153871.

[58] L. Ercole, R. Bertossa, S. Bisacchi, and S. Baroni, SporTran: a code to estimate transport coefficients from the cepstral analysis of a multi-variate current stationary time series, https://github.com/lorisercole/sportran (2017-2020).

[59] D. P. Kingma and J. Ba, Adam: A Method for Stochastic Optimization, 3rd International Conference on Learning Representations, ICLR 2015 - Conference Track Proceedings , 1 (2014), arXiv:1412.6980.

[60] M. L. V. Ramires, C. A. Nieto de Castro, Y. Nagasaka, A. Nagashima, M. J. Assael, and W. A. Wakeham, Standard Reference Data for the Thermal Conductivity of Water, Journal of Physical and Chemical Reference Data **24**, 1377 (1995).

[61] T. I. Gartner, L. Zhang, P. Piaggi, R. Car, A. Panagiotopoulos, and P. Debenedetti, Signatures of a liquid-liquid transition in an ab initio deep neural network model for water, http://arks.princeton.edu/ark:/88435/dsp01b5644v47m (2020).

[62] P. M. Piaggi, A. Z. Panagiotopoulos, P. G. Debenedetti, and R. Car, Phase equilibrium of water with hexagonal and cubic ice using the scan functional, Journal of Chemical Theory and Computation **17**, 3065 (2021).

[63] Nist chemistry webbook, https://webbook.nist.gov/chemistry/fluid/, accessed: 2020.

[64] In the Supplementary Material the two files can be found: kappa_T_DPMD-PBE.dat and kappa_T_DPMD-SCAN.dat. They contain the data points shown in Fig. 3 for the DPMD-PBE and DPMD-SCAN simulations, respectively. The files contain both 5 columns corresponding, respectively, to: average temperature, *kappa*, its statistical uncertainty, the value of $f^\star$ and the value of $P^\star$ chosen for the cepstral analysis.

[65] L. Stixrude, S. Baroni, and F. Grasselli, Thermal Evolution of Uranus with a Frozen Interior (2020), arXiv:2004.01756.

[66] F. Grasselli, L. Stixrude, and S. Baroni, Heat and charge transport in H2O at ice-giant conditions from ab initio molecular dynamics simulations, Nature Communications **11**, 3605 (2020).

[67] S. Plimpton, Fast parallel algorithms for short-range molecular dynamics, Journal of Computational Physics **117**, 1 (1995).

[68] A. P. Thompson, H. M. Aktulga, R. Berger, D. S. Bolintineanu, W. Michael Brown, P. S. Crozier, P. J. in 't Veld, A. Kohlmeyer, S. G. Moore, T. D. Nguyen, R. Shan, M. Stevens, J. Tranchida, C. Trott, and S. J. Plimpton, LAMMPS - A flexible simulation tool for particle-based materials modeling at the atomic, meso, and continuum scales, Computer Physics Communications , 108171 (2021).

[69] Lammps website, https://www.lammps.org.

[70] A more detailed description of the use of the LAMMPS interface for the energy current is given the DeePMD-kit documentation https://github.com/deepmodeling/deepmd-kit/blob/master/doc/third-party/lammps-command.md.

[71] I. Goodfellow, Y. Bengio, and A. Courville, *Deep Learning* (MIT Press, 2016) Chapter 6.

[72] D. E. Rumelhart, G. E. Hinton, and R. J. Williams, Learning representations by back-propagating errors, Nature **323**, 533 (1986).

[73] H. Wang, L. Zhang, J. Han, and W. E, DeePMD-kit: A deep learning package for many-body potential energy representation and molecular dynamics, Computer Physics Communications **228**, 178 (2018), arXiv:1712.03641.

[74] I. C. Yeh and G. Hummer, System-size dependence of diffusion coefficients and viscosities from molecular dynamics simulations with periodic boundary conditions, Journal of Physical Chemistry B **108**, 15873 (2004).

[75] M. Puligheddu and G. Galli, Atomistic simulations of the thermal conductivity of liquids, Physical Review Materials **4**, 053801 (2020).